JACS Au
AN OPEN ACCESS JOURNAL OF THE AMERICAN CHEMICAL SOCIETY

Open Access
This article is licensed under CC-BY-NC-ND 4.0

pubs.acs.org/jacsau
Article

Ultra-Low Optical Loss in Single Crystal Waveguides of Fluorene/Fluorenone Cd^{II} Coordination Polymers

Enrico Podda,* Massimiliano Arca, Anna Pintus, Vito Lippolis, Simon J. Coles, James B. Orton, Stefania Porcu, Pier Carlo Ricci, and M. Carla Aragoni*

Cite This: https://doi.org/10.1021/jacsau.4c00978
Read Online

ACCESS | Metrics & More | Article Recommendations | Supporting Information

ABSTRACT: Optical waveguides are essential components in integrated photonic circuits and communication devices. Despite recent advances in both inorganic and organic materials, the use of Coordination Polymers (CPs) as single-crystal optical waveguides remains in its infancy but shows great potential. This study aims to gain insight into several design factors for the preparation of single crystal CPs to be used as active optical waveguides. These factors include the nature of the ligand-based emission (investigated both experimentally and theoretically), chemical functionalization at the metal center with ancillary building blocks, and molecular arrangements within the crystal lattice. The CPs presented in this study demonstrate exceptional light propagation performances, with optical losses ranking among the lowest ever reported for CPs and single-crystal organic waveguides. The systematic comparison of the performance of the supramolecular assemblies presented here allowed us to draw significant conclusions, providing valuable insights for the future design of single crystal CPs and optimization of their optical waveguiding performance.

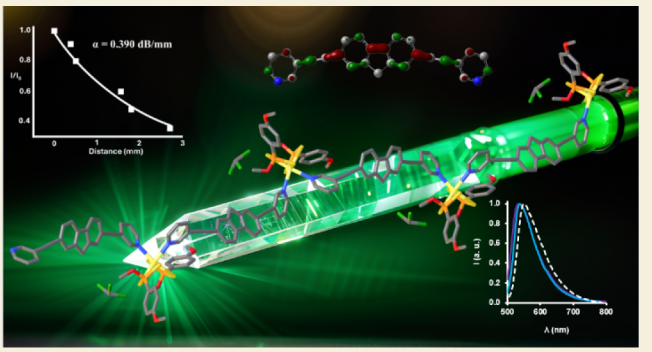

KEYWORDS: *single crystal waveguides, optical loss, coordination polymers, XRD, TD-DFT*

INTRODUCTION

Optical waveguides are fundamental components for the confinement and transmission of light over a range of distances, from tens or hundreds of micrometers within integrated photonics to hundreds or thousands of kilometers within long-distance fiber-optic communication.[1] Optical waveguide devices can be classified as either active or passive depending on their ability to either transduce photoluminescence (fluorescence or phosphorescence) or to direct wavelengths away from their optical absorption window, respectively.[2,3] While well-known silicon-based devices predominantly serve as passive waveguides, advanced inorganic and organic materials are suitable for both active and passive optical/optoelectronic applications that are highly sought after.[4−6] The development of these versatile materials, coupled with the study of elastic or plastic mechanical behavior of single crystals has sparked growing interest among the scientific community in leveraging these materials for advanced technological applications in biomedicine, flexible electronic devices, and optics.[7,8] To gain insight into the origins of crystal flexibility, recent approaches have been proposed based on the crystal packing and the study of supramolecular interactions.[9−11] The optical loss (OL) coefficient is a key parameter that reflects the potential of a novel material to be used as an optical waveguide.[12] It is influenced by a multitude of factors, including the intrinsic reabsorption of the material, the quality of the crystal, and the presence of structural defects. The OL has been investigated in flexible crystals, in both the straight and bent states, a poorer performance being observed in the latter case.[13] It should be noted that the emission wavelength of some organic crystals is red-shifted by increasing the distance from the excitation point to the opposite crystal terminus. This is a consequence of reabsorption phenomena, due to the limited Stokes shift between the absorption and emission profiles, which are partially overlapped.[14] The presence of noncovalent interactions, such as π-stacking and hydrogen bonding (HB), which often drive crystal packing, has been demonstrated to contribute significantly to light propagation. Indeed, flexible crystals exhibit increased OL in their flexed state due to the temporary lengthening of these interactions.[7,15,16] Among supramolecular interactions, coordination bonds implemented in Coordination Polymers (CPs) have recently emerged as an alternative to pure organic

Received: October 17, 2024
Revised: November 27, 2024
Accepted: November 27, 2024

Downloaded via 82.11.180.11 on February 11, 2025 at 10:43:39 (UTC).
See https://pubs.acs.org/sharingguidelines for options on how to legitimately share published articles.

ACS Publications
© XXXX The Authors. Published by American Chemical Society

Scheme 1. Synthetic Pathways Followed for the Preparation of the Luminescent CPs Presented in This Work[a]

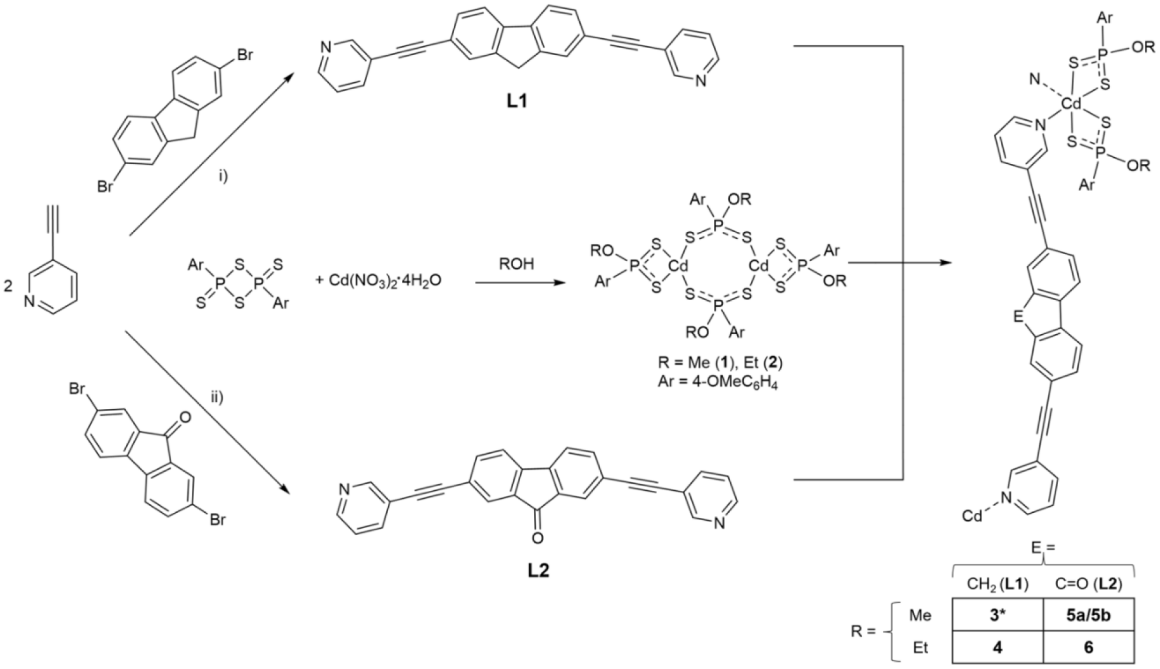

[a]i) $Pd(PPh_3)_2Cl_2$, CuI, toluene/Et_2NH, N_2; (ii) $Pd(PPh_3)_2Cl_2$, CuI, Et_2NH, N_2 from ref 29. * CP **3** was isolated as a chloroform solvate.

crystals. However, their use as optical waveguides remains limited. In this context, the self-assembly of metal halides (M = Cu^I, Cd^{II}) with pyridyl derivatives resulted in the formation of several CPs that exhibit anisotropic flexibility and good optical waveguiding performance.[13,17] Additionally, the development of an active red-emitting optical waveguide based on an Eu^{III}–CP indicated a potential implementation within optical devices.[18] However, further optimization for the use of single crystal CPs as optical waveguides is necessary as well as a more detailed investigation of the structure-performance relationships.

Fluorene derivatives have been widely adopted in the preparation of both charged or neutral building blocks in supramolecular chemistry.[19−22] Their main features are exemplified by the extensive range of emission wavelengths that can be obtained and tailored to specific applications. Neutral fluorene-based ligands functionalized with pyridyl[21−23] or imidazolyl[24−27] moieties have frequently been employed in conjunction with ancillary ligands, such as carboxylic acids, to bind naked metal ions or clusters in the self-assembly of CPs or Metal Organic Frameworks (MOFs). Following our previous reports on fluorene derivatives,[20,28,29] we have designed two novel luminescent donors, namely 2,7-bis(pyridin-3-ylethynyl)-9H-fluorene (**L1**) and 2,7-bis(pyridin-3-ylethynyl)fluoren-9-one (**L2**), containing two *meta*-substituted pyridyl-ethynyl moieties linked by either a 9H-fluorene or a fluoren-9-one core (Scheme 1).

Dithiophosphonato metal complexes have been demonstrated to be optimal building blocks for the predictable assembly of CPs, due to their coordinative instauration that facilitates a transition from tetra- to hexa-coordination at the metal ion.[30,31] In particular, dithiophosphonato cadmium(II) complexes are dimers in which both metal ions share a tetrahedral coordination, as shown in Scheme 1,[32] and are capable of reacting with the pyridyl moieties of **L1** and **L2** to form octahedral complexes. In addition, the 4-methoxyphenyl substituents have been demonstrated to regulate the secondary assembly by participating in different packing interactions contingent on their nature.[33,34] It is noteworthy that, despite the large number of reports on complexes between dithiophosphonates and a variety of metals from the periodic table,[35] only a limited number of studies explored the incorporation of dithiophosphonato complexes into luminescent materials.[36−39] Given the absence of precedents for the application of dithiophosphonato-based CPs as single-crystal optical waveguides, we decided to prepare a series of Cd^{II}–CPs by reacting **L1** and **L2** with the two coordinatively unsaturated bis(O-alkyl)(4-methoxyphenyl)phosphonodithioato)-cadmium(II) complexes [Cd(RO-dtp)$_2$; R = Me (**1**), Et (**2**)]. The objective was to investigate the factors that can be employed to optimize the relative performance of the obtained CPs (**3**–**6**) as active optical waveguides. These factors include the emission of the free and complexed ligand, which was investigated both experimentally and theoretically. The emission was tuned by varying the chemical functionalization at the metal center with auxiliary components and by modifying the molecular arrangement within the crystal structure. The results demonstrated remarkable light propagation capabilities, with OL among the lowest ever recorded for CPs and single-crystal organic waveguides.

RESULTS AND DISCUSSION

Synthesis

The ligand 2,7-bis(pyridin-3-ylethynyl)-9H-fluorene (**L1**) was designed with two pyridylethynyl groups connected by a 9H-fluorene core, by following the methodology outlined in our previous report on **L2** (the analogous oxidized counterpart of **L1**, in which the 9H-fluorene is replaced by a fluoren-9-one moiety; Scheme 1).[29] Both ligands feature *meta*-substituted pyridyl fragments that can assume three planar reciprocal orientation affording: two periplanar conformers with the lone

https://doi.org/10.1021/jacsau.4c00978
JACS Au XXXX, XXX, XXX−XXX

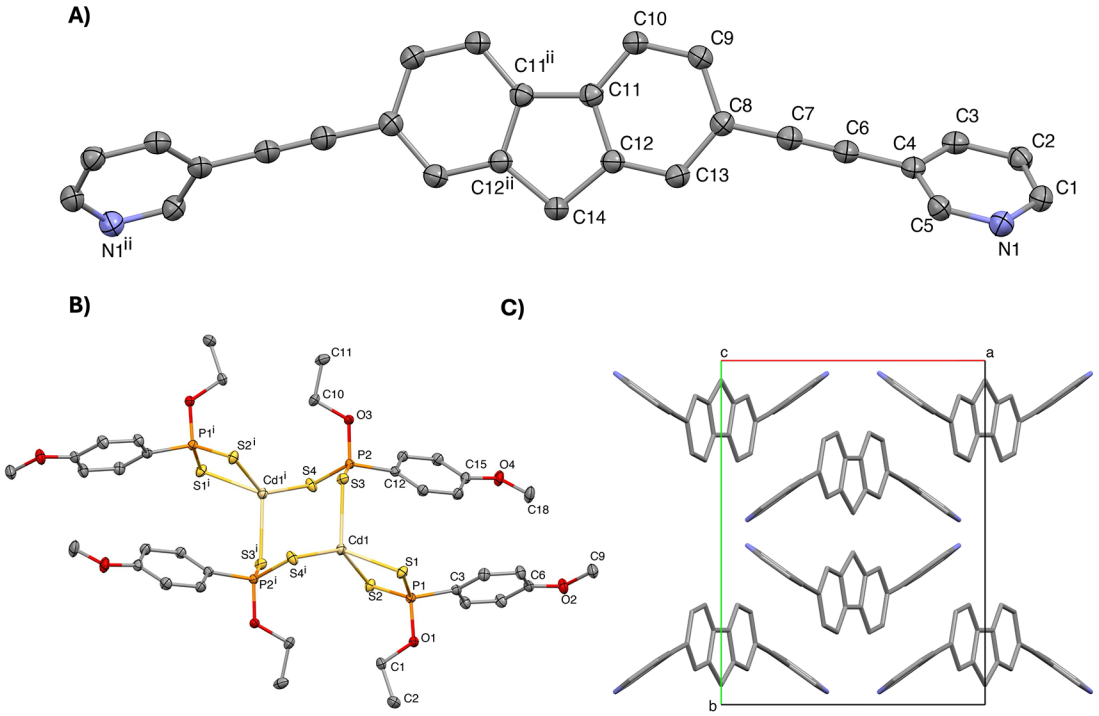

Figure 1. X-ray crystal structures of **L1** (A) and 2 (B). Displacement ellipsoids are drawn at the 50% probability level. Packing view of **L1** along the [001] direction (C). Symmetry codes: i = 1−*x*, −*y*, 1−*z*; ii = −*x*, −*y*, 1/2−*z*.

pair of electrons on the nitrogen atoms pointing in the same direction and an antiperiplanar arrangement with the pyridyl rings pointing to opposite directions. It is worth noting that previous studies reported the syntheses of analogous derivatives with *para*-substituted pyridyl moieties such as 2,7-bis(pyridin-4-ylethynyl)-9,9-diethylfluorene. These were incorporated into intriguing CPs with chiral square-grid and triple-helix structures.[21,22] The syntheses of **L1** and **L2** were carried out in a single step by means of a Sonogashira cross-coupling reaction between 3-ethynylpyridine and 2,7-dibromofluorene or 2,7-dibromofluoren-9-one, respectively. The synthesis of complexes **1** and **2** was carried out by reacting Lawesson's reagent and $Cd(NO_3)_2{\cdot}4H_2O$ in the relevant solvent, namely MeOH for complex **1** and EtOH for complex **2**.[35] To construct new luminescent cadmium(II)-based CPs, **L1** and **L2** were reacted with the dithiophosphonato complexes *bis*[*O*-alkyl(4-methoxyphenyl)dithiophosphonato]-cadmium(II) [Cd(RO-dtp)$_2$; alkyl group *R* = Me (**1**), Et (**2**), Scheme 1] in 1:1 and 1:2 (v/v) alcohol/chloroform solvent mixtures, affording a series of five luminescent CPs **3**, **4**, **5a**, **5b**, and **6** (Scheme 1).

Structural Characterization

Pale-yellow crystals were successfully grown from an ethanol solution of **L1**. The organic donor crystallizes in monoclinic space group *C*2/*c* with half of the molecule in the asymmetric unit (Figure 1A and Table S1). The *pseudo*-rigid ligand exhibited a nonplanar structure, with fluorenyl groups aligned along the *b*-axis and pyridyl rings twisted by about 72° with respect to the fluorene core, resulting in an intramolecular N···N distance of 18.72 Å. The **L1** units pack through intermolecular edge-to-face $\pi-\pi$ interactions (Figure S1) and weak CH···N hydrogen bonds (HBs) between symmetry-related pyridyl moieties with pyridyl rings aligned along the *c*-axis (Figure S2). It is worth noting that the structural characterization of **L2**, reported in our previous work,[29] showed a rather different packing scenario with a monoclinic primitive lattice (space group $P2_1/c$) in which **L2** molecules were packed by a combination of strong face-to-face $\pi-\pi$ interactions and HBs of the types CH···O and CH···N.

The recrystallization from an ethanol solution of complex **2** yielded colorless crystals. The complex displays a dimeric arrangement (Figure 1B) similar to that previously reported in the literature for analogous dithiophosphonato metal complexes (see Tables S2 and S3 for a comprehensive comparison of analogous Cd^{II} complexes).

The reaction of **L1** with **1** in a 1:1 MeOH/$CHCl_3$ (*v*/*v*) mixture yielded CP **3** as colorless, plate-like crystals, which were harvested from the solution and structurally characterized. An X-ray diffraction (XRD) analysis indicates that CP **3** belongs to the monoclinic noncentrosymmetric space group *Cc* (Table S1 and Figure 2) with an asymmetric unit populated by a Cd^{II} ion, an **L1** molecule, two dithiophosphonato anions derived from the starting complex **1**, and a cocrystallized chloroform molecule (Figure 2A). The central Cd^{II} ion shows a *pseudo*-octahedral coordination geometry in CP **3**, resulting from the rearrangement of the two dithiophosphonato anions and the additional *cis*-coordination by the pyridine nitrogen donor atoms N1 and $N2^i$ belonging to two symmetry-related **L1** ligands (Figure 2A).

The geometric features of the coordination sphere are similar to those previously reported for analogous Cd^{II}- based CPs (Table S2).[40] In the crystal structure of CP **3**, the donor **L1** bridges two metal centers by adopting an antiperiplanar conformation that generates a sinusoidal zigzag motif that propagates perpendicular to the *b*-axis with a periodicity of 42.3 Å and $Cd1\cdots Cd1^{ii}$ distances of 22.0 Å (Figure 2B). The peculiar nonplanar conformation of **L1** results in a swinging motion of the fluorenyl groups, which alternately project inward and outward with respect to the direction of propagation of the zigzag chain motif (Figure 2B). The crystal

https://doi.org/10.1021/jacsau.4c00978
JACS Au XXXX, XXX, XXX−XXX

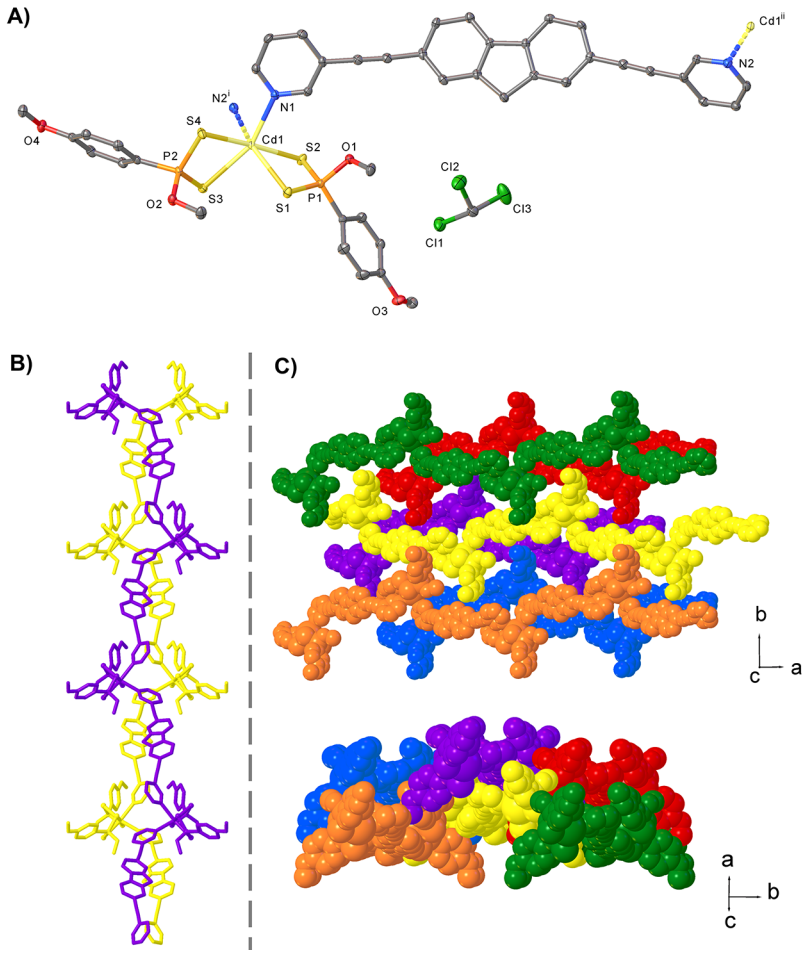

Figure 2. X-ray crystal structure of CP **3**: asymmetric unit with the numbering scheme adopted for heteroatoms only. Displacement ellipsoids are drawn at 50% probability level (A). Symmetry codes: ^{i} = −1+*x*, 1−*y*, − 3/2+*z*; ^{ii} = 1+*x*, 1−*y*, 3/2+*z*; a pair of interwoven zigzag chains (B); partial views of the crystal packing (C).

packing shows a complex entanglement between staggered zigzag chains (Figure 2C), with interchain $\pi-\pi$ stacking interactions between fluorenyl and pyridyl rings (Figure S3) and intermolecular HBs involving the O atoms and the aromatic protons of both fluorenyl and pyridyl rings (Figure S4 and Table S4).

The reaction between **L1** and **2** in a 1:2 ethanol/chloroform (*v*/*v*) mixture afforded pale-yellow needle-shaped crystals of CP **4**, whose crystal structure was determined by XRD analysis. CP **4** crystallizes in the monoclinic centrosymmetric space group $P2_1/c$ (Table S1) with the asymmetric unit consisting of one Cd^{II} ion, one **L1** molecule, and two ethoxy-substituted dithiophosphonato ligands, closely analogous to that just described for CP **3** (Figure S5).

The structure of CP **4** is similar to that of CP **3**, with a central Cd^{II} ion coordinated in a *pseudo*-octahedral geometry by two η^2-chelating dithiophosphonato anions originated from complex **2** and two nitrogen atoms from symmetry-related **L1** ligands (Figure S5). The corresponding bond lengths and angles determined for both CPs are very close to each other (Table S2), as are the sinusoidal zigzag chains with almost identical Cd···Cd distances and periodicity, 21.99(2) and 21.91(2) Å, and 42.29(2) and 41.91(2) Å for CPs **3** and **4**, respectively (Figure S5). Despite the absence of cocrystallized solvent molecules, the crystal packing of CP **4** exhibits interactions similar to those observed in CP **3** (Figure S5). The phase purity of the bulk samples of CPs **3** and **4** was confirmed by powder XRD (PXRD) analysis by comparing the experimental pattern collected on the hand-grinded compound with the calculated pattern derived from the single-crystal XRD data (Figures S6 and S7). The comparable geometric features of **L1** and **L2** prompted us to investigate whether the sinusoidal zigzag assemblies observed in CPs **3** and **4** could be obtained by replacing **L1** with its oxidized counterpart, **L2**. The reaction of **L2** with **1** resulted in the formation of two clearly distinguishable crystalline products, CPs **5a** and **5b**, each of which exhibited distinct morphologies that were readily discernible under an optical microscope (Figure 3). Single-crystal XRD analysis revealed that CPs **5a** and **5b** are polymorphic species. In particular, CP **5a** is isostructural with CP **4** and CP **6** (see below), whereas CP **5b** showed a distinct crystal structure (Figure 3, Tables S1 and S2). Notably, both CPs **5a** and **5b** crystallized in the same space group $P2_1/c$, with different lattice parameters *a* and *c* but similar *b* lengths and β angles (Figure 3 and Table S1), with identical atomic connectivity and supramolecular motif but differing significantly for the geometric features of **L2** and one of the aromatic dithiophosphonato moieties (Figures S18 and S19). The

https://doi.org/10.1021/jacsau.4c00978
JACS Au XXXX, XXX, XXX−XXX

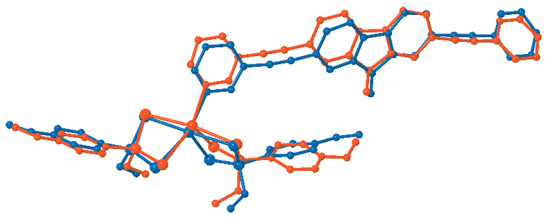

	5a	5b
Space Group	$P2_1/c$	$P2_1/c$
a (Å)	15.9160(13)	19.6053(17)
b (Å)	22.6324(19)	22.952(2)
c (Å)	12.5429(9)	9.9323(8)
α, γ (°)	90	90
β (°)	106.088(3)	104.197(3)
V (Å^3)	4341.2(6)	4332.9(6)

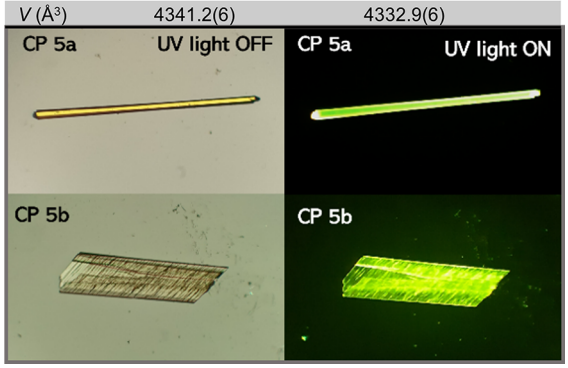

Figure 3. View of the overlaid crystal structures of polymorphs CPs **5a** and **5b** and their lattice parameters. Images of crystals of CPs **5a** and **5b** under polarized light and UV irradiation.

superimposed asymmetric units for both crystal structures of CPs **5a** and **5b** are depicted in different colors and are shown in Figure 3 together with the relevant lattice parameters and the optical photographs of the corresponding crystals under polarized light, with and without UV illumination. Consistent with our observation, previous studies have shown that small geometric changes in the crystal lattice can induce non-negligible variations in the crystal morphologies of pyridyl Cd^{II}-based CPs.[17]

The PXRD analysis of the bulk material confirmed the presence of the two crystalline products CPs **5a** and **5b**, which were obtained simultaneously from the crystallization setup (Figure S8). Crystals of **5b** were manually selected under an optical microscope and their XRD pattern (Figure S9) confirmed the presence of **5b** as the only phase. This solid was used to compare the spectroscopical properties of the "as-synthesized" mixture (CPs **5a** and **5b**) with pure CP **5b** (see below).

The reaction between **L2** and complex **2** in a 1:1 EtOH/$CHCl_3$ (v/v) mixture yielded yellow rod-shaped crystals after slow evaporation of the solvent. Single crystal XRD analysis established the product as CP **6** which was found to be isostructural with CP **4** and CP **5a**, sharing the zigzag motif described previously (Table S1 and Figure S20). The PXRD analysis confirmed CP **6** as the only crystalline phase present in the bulk of pure material (Figure S10). The comparison of the geometric features observed for both the free and the coordinated donors **L1** and **L2** in the CPs demonstrates that **L1** and **L2** are capable of adopting different torsion angles, thereby enabling structural adaptability to ancillary ligands or solvents (Table S5). This flexibility is a crucial attribute, as it indicates that **L1** and **L2** consent to the predictable assembly of polymeric networks, thereby facilitating more controlled and tunable architectures in CPs design.

Absorption and Emission Spectroscopies

The absorption and emission photoluminescent (PL) properties of **L1** and **L2** were investigated in solution and in the solid state for **L1**, **L2**, and derived CPs **3**−**6**. Notable differences are observed in the absorption spectra of **L1** and **L2** in a $CHCl_3$ solution (Figure S11). The UV−vis spectrum of **L1** displays a single, highly structured absorption peak at 351 nm (ε = 72400 M^{-1} cm^{-1}), which upon excitation results in emission at 433 nm. **L2** exhibits three absorption maxima: the two most

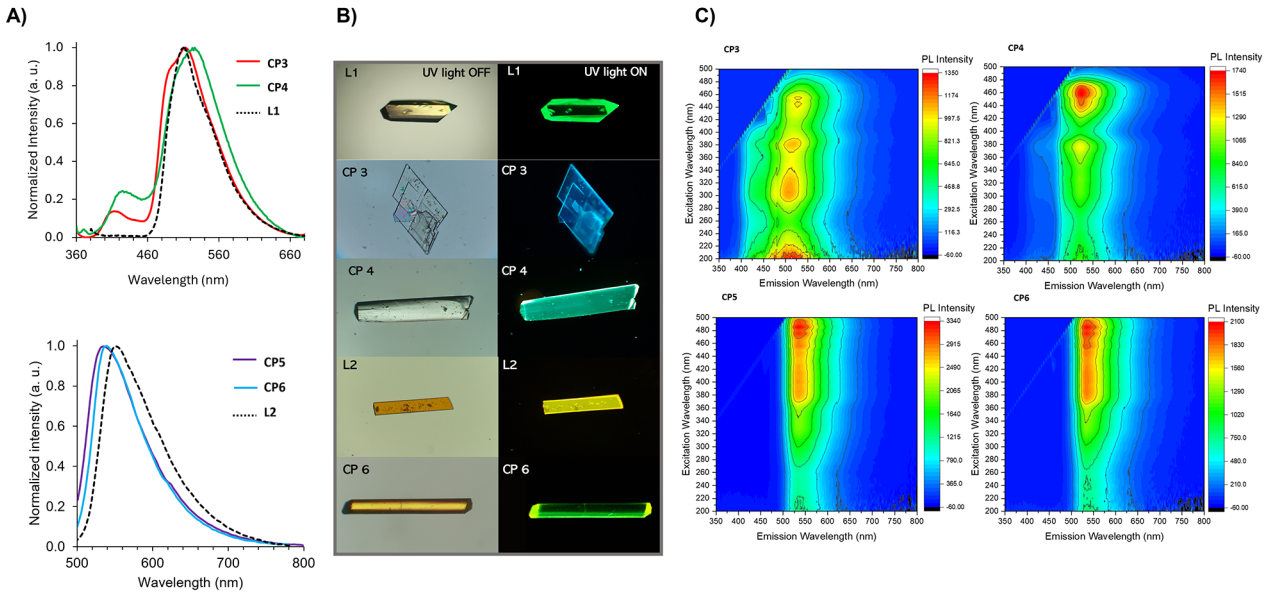

Figure 4. Photoluminescence emission properties in the solid state: emission profiles (A) and photographs of microcrystals under polarized light and UV illumination (B); photoluminescence (PLE) excitation/emission maps recorded at room temperature on CPs presented in this work (C).

https://doi.org/10.1021/jacsau.4c00978
JACS Au XXXX, XXX, XXX−XXX

intense ones at 305 and 353 nm (ε = 72300 and 45300 M^{-1} cm^{-1}, respectively) and a much less intense one at 466 nm (ε = 3500 M^{-1} cm^{-1}). Upon excitation within the range of 250−450 nm, an emission at 555 nm was observed.

The solid-state absorption and emission properties of **L1**, **L2**, and the resulting CPs were subjected to a comprehensive investigation (Figures 4 and S12). The fluorene derivative **L1** exhibits a strong broad absorption in the UV region with the main excitation peak at 380 nm, resulting in a sharp emission at 514 nm. Photoluminescence Excitation/Emission (PLE) maps, emission profiles, and solid-state absorption spectra allow to evidence of similarities and differences in the electronic spectroscopic properties of **L1** and the CPs **3** and **4**. The emission spectra of the three related compounds **L1**, CP **3**, and CP **4** are fairly similar; however in addition to the main band centered at approximately 515 nm, a less intense but more energetic emission is observed at 408 nm, and it is noteworthy that the emission profile of CP **3** is broader as compared to **L1** and CP **4** (Figure 4C). In particular, the main band is composed of the convolution of two contributions centered at 490 and 512 nm (Figure 4A). These differences can be tentatively attributed to the different crystal packings and crystal space groups of CP **3** compared to the other CPs. In contrast with **L1** and CP **3**, whose main excitations are featured in the range 300−380 nm, the PLE map of CP **4** shows a novel, highly intense region at 450 nm (emission at 520 nm), which represents its main excitation pathway.

Upon excitation at 490 nm, **L2** shows a strong emission at 554 nm, coincident with that observed in the $CHCl_3$ solution. In the resulting CPs **5a−b** and **6**, this emission is blue-shifted to 540 nm. To assess the emission properties of CPs **5a** and **5b**, crystals of both polymorphs were manually selected, and their emission spectra were recorded, revealing no significant variations. The PL emission spectrum reported in Figure 4 was collected on the "as-synthesized" sample, which contains both polymorphs. In contrast to CPs **3** and **4**, the emission spectra of the fluorenone-based CPs did not show any additional bands within the range 400−460 nm. Their PL emission at 540 nm could be successfully obtained upon excitation in the range of approximately 380−480 nm, where their absorption peaks were observed in the PLE experiments. Time-resolved fluorescence studies for ligands **L1** and **L2**, and isostructural CPs **4**, **5a**, and **6** revealed comparable results, with fluorescence lifetimes in the nanosecond regime (Figure S13).

DFT Calculations

Theoretical calculations on PL properties are becoming an increasingly popular area of research. This notwithstanding, these types of quantum-mechanical calculations are not easy to perform, requiring the optimization of the geometry of the excited states involved in the absorption and in the relaxation processes.[41] The use of time-dependent density functional theory (TD-DFT) calculations for this task is exemplified by the recently reported solid-state fluorescent properties of a new bifluorene−tetracarboxylic acid and its supramolecular assemblies, which were elucidated at this level of theory.[20] In order to validate a reliable yet affordable computational setup, the absorption and emission properties of fluorene and fluorenone were separately evaluated. These compounds show a typical absorption at λ_{abs} = 261 and 382 nm, respectively, in cyclohexane.[42] Upon excitation at the same wavelength, fluorescent emission is observed at λ_{fluo} = 302 and 463 nm, respectively. The geometry of both compounds was optimized by using the PBE0 functional[43] and adopting two sets of basis functions (BS), namely the Def2SVP basis,[44] a split-valence basis set with polarization functions, and the triple-ζ 6−311+G belonging to the well-known Pople family of BSs.[45−48] Cyclohexane solvation was taken into account with the Polarizable Continuum Model using the Integral Equation Formalism variant (IEF-PCM) Self-Consistent Reaction Field (SCRF) method.[47] The lowest-energy absorption bands were correctly calculated for fluorene and fluorenone at the TD-DFT level with both BSs (Table 1), and attributed to the singlet vertical transition to the first excited state (ES#1), involving mainly the Kohn−Sham HOMO → LUMO $\pi \rightarrow \pi^*$ one-electron vertical excitation (39% for fluorene, 100% for fluorenone). The geometries of the involved ESs were optimized and the emission wavelengths λ_{fluo} in cyclohexane solution were calculated, neglecting zero-point-energy (ZPE) corrections, from the relaxation energies (E_{fluo}) at 300 and 299 nm for fluorene, and at 499 and 526 nm for fluorenone by adopting the Def2SVP and 6−311+G BSs, respectively (Table 1). Therefore, while the emission energy (E_{fluo}) was calculated reliably in the case of fluorene, in the case of fluorenone a slight underestimation of E_{fluo}, corresponding to an overestimation of the corresponding Stoke shift, was obtained (Table 1).

Table 1. Experimental and TD-DFT-Calculated (Def2SVP and 6-311+G Basis Sets) Fluorene, Fluorenone, L1 and L2 in Solution at SCRF IEF-PCM Level[a]

		Fluorene[b]	Fluorenone[b]	L1[c]	L2[c]
E_{abs}	Exp.	4.750	3.246	3.532	2.780
	Def2SVP	4.673	3.340	3.247	2.687
	6−311+G	4.694	3.147	3.354	2.592
λ_{abs}	Exp.	261	382	380	446
	Def2SVP	265.3	371.2	381.8	461.5
	6−311+G	264.1	394.0	369.8	478.2
E_{fluo}	Exp.	4.106	2.678	2.864	2.234
	Def2SVP	4.136	2.485	2.822	2.100
	6−311+G	4.153	2.358	2.905	1.977
λ_{fluo}	Exp.	302	463	433	555
	Def2SVP	299.8	498.9	439.3	590.6
	6−311+G	298.6	525.8	426.9	627.3
E_{adia}	Def2SVP	4.423	2.885	3.039	2.398
	6−311+G	4.447	2.762	3.134	2.290
λ_{adia}	Def2SVP	280.3	429.8	408.0	517.0
	6−311+G	278.9	449.0	395.6	541.5
Stokes shift	Exp.	41	81	82	109
	Def2SVP	34.5	127.8	57.5	129.1
	6−311+G	34.4	131.8	57.1	149.1

[a]Lowest transition energies (E_{abs}, eV) and corresponding absorption wavelength (λ_{abs}, nm), fluorescent emission energy (E_{fluo}, eV), corresponding emission wavelength (λ_{fluo}, nm), adiabatic excitation energy (E_{adia}, eV), corresponding excitation wavelength (λ_{adia}, nm), and Stokes shift values (nm). [b]Cyclohexane solution. [c]Chloroform solution.

The frontier molecular orbitals (MOs) for ligands **L1** and **L2** are summarized in Table 1 and Figure 5A. The vertical excitation and relaxation paths for **L1** are presented in Figure 5B. The lowest-energy vertical transition for **L1** at the TD-DFT level is calculated to occur at λ_{abs} = 371 nm in the gas phase and 382 nm in $CHCl_3$ (oscillator strength f = 2.25 and 2.49, respectively) at the PBE0/Def2SVP level (PBE0/6−

https://doi.org/10.1021/jacsau.4c00978
JACS Au XXXX, XXX, XXX−XXX

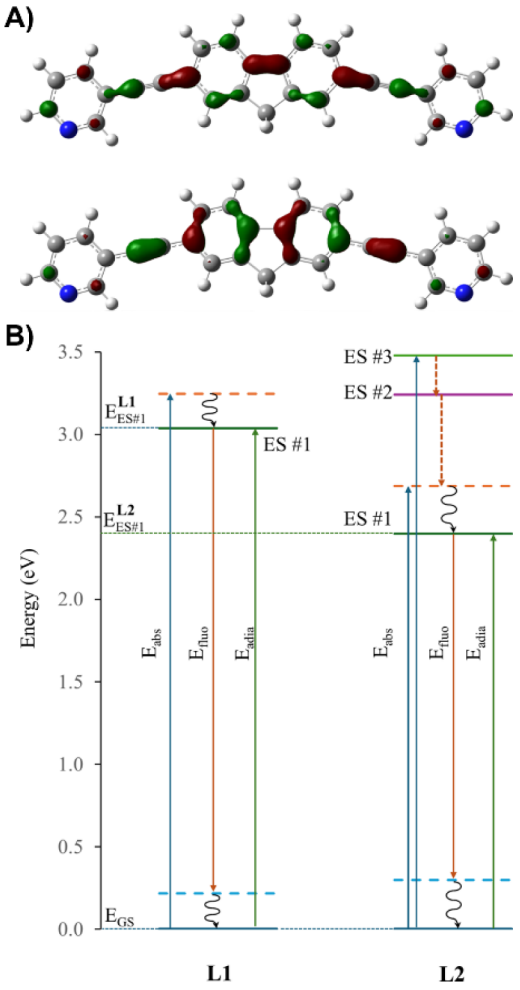

Figure 5. Isosurfaces of KS-HOMO (bottom) and KS-LUMO (top) calculated in $CHCl_3$ for **L1** at the PBE0/Def2SVP level in the periplanar conformation (cutoff value = 0.05 |e|) (A); quantitative relative energy diagram for the vertical absorption (blue arrows), adiabatic excitation (green arrows), and fluorescence emission (orange arrows) processes calculated for **L1** and **L2** in $CHCl_3$ solution (B). E_{GS} and E_{ES} are the minimum energies of the ground and excited states, respectively.

311+G: λ_{abs} = 359 and 370 nm, respectively; Tables 1 and S6). These values, very close to each other, are in good agreement with the broad absorption shown in the solid state up to 380 nm and with the absorption at 351 nm in $CHCl_3$ (see above). In all cases, this transition can be ascribed entirely to a one-electron excitation between the KS-HOMO and the KS-LUMO (Figure 5A), which are KS-MOs π-in-nature delocalized over the whole molecule and largely involving the fluorene core of **L1**. Since the KS-LUMO is bonding with respect to the C−C bond of the fluorene pentatomic ring (C11−C11^{i} in Figure 1A; C11−C16 in Table S5) and antibonding with respect to the −C≡C− bond of the pyridin-3-yl-ethynyl moieties, the optimized geometry of the excited states displays a shorter C−C bond (GS: 1.460; ES#1: 1.415 Å) and longer −C≡C− bond distances (GS: 1.220; ES#1: 1.235 Å). The corresponding adiabatic excitation wavelength (λ_{adia}) is calculated at 408 nm at the PBE0/Def2-SVP level (6−311+G BS: 396 nm; Table 1) in agreement with the excitation peak observed at 380 nm (see above). The fluorescence emission energy (E_{fluo}) was calculated to occur at 2.984 and 2.822 eV, in the gas phase and $CHCl_3$, respectively, corresponding to a visible emission wavelength λ_{fluo} centered at 416 nm in the gas phase and 439 nm in $CHCl_3$ (λ_{fluo} = 404 and 427 nm at PBE0/6−311+G level, respectively; Tables 1 and S6).

The excitation and relaxation path calculated for **L2** is comparable to that of **L1**, the narrower HOMO−LUMO energy gap of the former resulting in largest absorption (λ_{abs}), adiabatic excitation (λ_{adia}), and emission (λ_{fluo}) wavelengths (Tables 1 and S6). The lowest electronic transition (GS → ES#1; E_{abs} = 2.688 eV, λ_{abs} = 461 nm, f = 0.468 at PBE0/Def2SVP level) involves the π−π* HOMO→LUMO excitation, while the more intense absorptions in the range 300−350 nm can be attributed to the transitions to the ES#3 (E_{abs} = 3.478 eV, λ_{abs} = 357 nm, f = 1.701) and ES#7 (E_{abs} = 4.125 eV, λ_{abs} = 301 nm, f = 0.823), mainly involving the HOMO−1 → LUMO and HOMO−5 → LUMO excitations, respectively (Figure S15). Analogous to **L1** and due to the similar composition of frontier MOs (Figure S14), the GS → ES#1 transition calculated for **L2** results in a shortening of the C11−C16 distance (Table S5) in the pentatomic ring of the fluorenone core (GS: 1.474; ES#1: 1.413 Å) and a lengthening of the −C≡C− bond of the pyridin-3-yl-ethynyl arms (GS: 1.219; ES#1: 1.226 Å).

Since the experimental emission energy is independent of the excitation wavelength (see above), it can be inferred that whatever the ES involved upon excitation (ES#1, ES#3, ES#7; Figure S15), a vibrational relaxation leads to ES#1 from which the fluorescence emission occurs (Figure 5B). The fluorescence emission energy for **L2** was calculated at E_{fluo} = 2.190 and 2.100 eV, in the gas phase and $CHCl_3$, respectively, corresponding to a visible emission centered at λ_{fluo} = 566 nm in the gas phase and 591 nm in $CHCl_3$ (591 and 627 nm at the PBE0/6−311+G level, respectively; Tables 1 and S6).

Therefore, a comparison of experimental and theoretical data shows that excellent agreement holds between experimental and TD-DFT calculated PLE spectra in $CHCl_3$ solution. The best agreement is achieved for **L1** (with E_{fluo} values within 1.5% from experimental emission energy with both BSs), while for **L2** a larger difference is found, the best agreement (6%) being obtained with the Def2SVP BS.

Solid-state emission energies can be compared with the corresponding E_{fluo} values calculated in the gas phase. TD-DFT calculations tend to overestimate the emission energy for **L1**, while excellent agreement is found for **L2**.

Based on the results obtained for **L1** and **L2**, theoretical calculations were extended to the corresponding CPs. As model compounds, monomeric units with formula [Cd(**L1**)$_2$(EtO-dtp)$_2$] (**7**) and [Cd(**L2**)$_2$(EtO-dtp)$_2$] (**8**) were considered and starting from the structural data, their geometries optimized in the gas phase (Figure S16 for [Cd(**L1**)$_2$(EtO-dtp)$_2$]). The coordination geometry at the metal ion was reproduced correctly for both model complexes, with very good agreement in the Cd−N and Cd−S bond distances [**7**: average Cd−N: 2.457(9) Å; Cd−S: 2.727(12) Å; **8**: average Cd−N: 2.464 Å; Cd−S: 2.722(18) Å].

A natural population analysis at the optimized geometry shows that the complex formation results in transfers of 1.184 and 1.181 |e| from the ligands to the Cd^{II} ion in **7** and **8**, respectively. The coordinative bonds are strongly polarized, with average Wiberg bond indexes[51] of 0.15 and 0.37 for Cd−N and Cd−S bonds, respectively. Worthy of note, in the complexes, the two P−S bonds of each dithiophosphonato

https://doi.org/10.1021/jacsau.4c00978
JACS Au XXXX, XXX, XXX−XXX

ligand feature very close Wiberg bond indexes (1.21 and 1.16), in agreement with the isobidentate coordination geometry. In Figure 6, the isosurfaces of selected frontier KS-MOs are depicted for **7**. Worthy of note, the Cd^{II} ion contributes significantly to KS-HOMO, while the remaining MOs are entirely ligand centered. As discussed above, the solid-state diffuse reflectance spectra of CPs **4** and **6** closely recall those of parent ligands **L1** and **L2** (Figure S12). The lowest allowed vertical transition for complex **7** is calculated at 381 nm (f = 4.137), i.e., very close to the corresponding λ_{abs} value calculated for **L1**. This transition (GS → ES#3) results from vertical excitations involving the uppermost occupied KS-MOs and the LUMO/LUMO+1, while no contribution from the KS-HOMO, and hence from the Cd^{II} ion, occurs. The largest contributions involve KS-HOMO−1 → KS-LUMO+1 (29.5%), KS-HOMO−2 → KS-LUMO+1 (23.3%), and KS-HOMO−3 → KS-LUMO (17.8%) one-electron excitations. An inspection of the composition of these MOs (Figure 6) clearly shows that KS-HOMO−2 and KS-HOMO−1 are mainly contributed from the KS-HOMO of **L1**, while KS-LUMO and KS-LUMO+2 are from the KS-LUMO of **L1**. Analogously, the allowed vertical transitions for complex **8** (GS → ES#2 and GS → ES#4) at the lowest energy are calculated at 464 and 457 nm (f = 0.167 and 0.292, respectively), again very close to the corresponding λ_{abs} value calculated for **L2** (Table S6). Even in the case of model complex **8**, the absorption is due to the excitations involving KS-MOs localized on the **L2** ligand. These results can be generalized to the other CPs and it can be inferred that the excitations contributing to the vertical transitions responsible for the broad intense visible absorption in the Cd^{II}-based CPs under consideration are ligand-centered and involve the same HOMO−LUMO excitation responsible for the visible absorption of free ligands **L1** and **L2**. Consequently, the same KS-MOs are involved in relaxation processes, so that the emission processes can also be considered as well as ligand-centered in nature, and account for the similar experimental behavior of the ligands and the corresponding CPs.

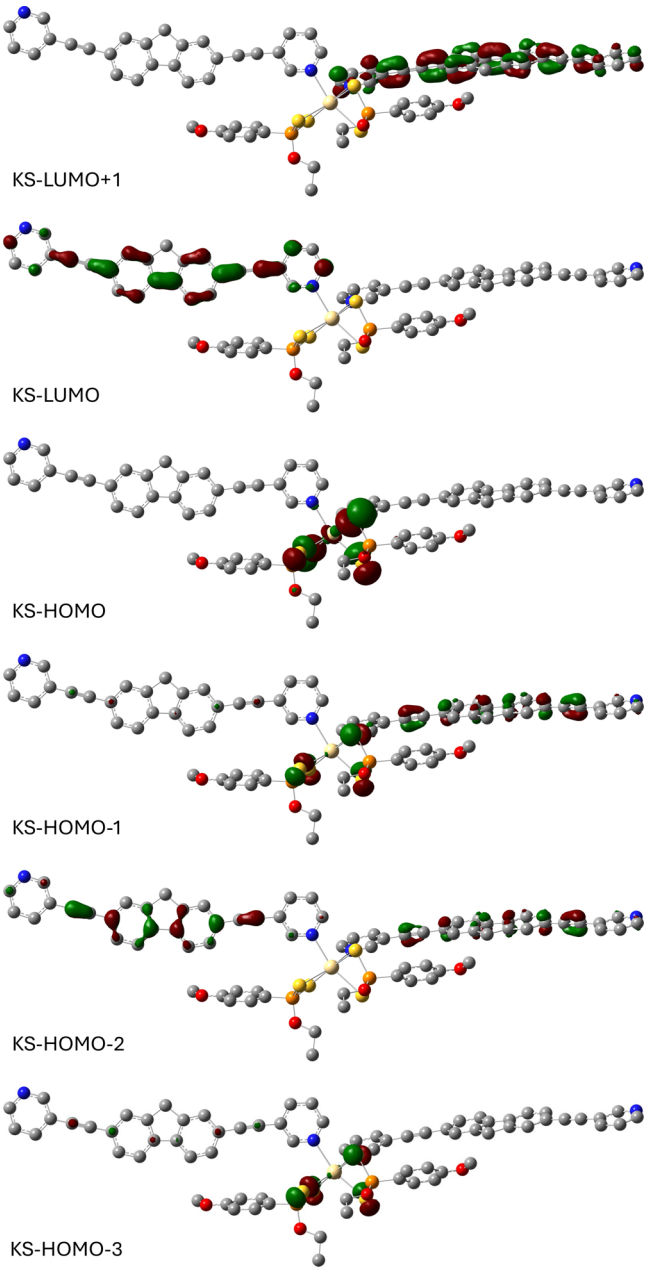

Figure 6. Isosurfaces of frontier KS-MOs calculated for complex $[Cd(\mathbf{L1})_2(EtO\text{-}dtp)_2]$ (**7**) at the PBE0/Def2SVP level. Cutoff value = 0.05 lel.

Optical Waveguiding Properties

The performance of optical waveguides can be described by several distinct characteristics. Among these, optical loss (OL) is particularly diagnostic and is typically evaluated by the OL coefficient (α_{dB}), which should be as low as possible. Given the aforementioned properties of PL, an evaluation of the optical waveguiding performance was conducted directly on microrod crystals of CPs **4**, **5a**, **5b**, and **6**. CP **3** was deemed unsuitable for inclusion in this study due to a number of factors: (i) its solvate nature, precluding a direct comparison to the other CPs presented herein; (ii) its morphology (stacked-plates, see Figure 4B), differing significantly from that of the other CPs; (iii) its broader luminescence emission. With regard to the other CPs, a gradual decrease in PL intensity was observed at the terminal face of the crystals as their length increased and the distance from the excitation point to the terminal point increased (assuming homogeneity among the single crystals). Accordingly, the α_{dB} values for CPs **4**, **5a**, **5b**, and **6** were estimated from distance-dependent PL spectra (Figure 7), according to the literature,[2] and ranged between 0.390 and 0.875 dB mm^{-1}. A direct comparison between CPs **4** and **6** (featuring the same ethoxy-substituted dithiophosphonato moiety and differing in the presence of **L1** and **L2** donors, respectively) shows a reduction in α_{dB} values by approximately 37% on passing from CP **4** to **6**. This suggests that fluorenone promotes a more efficient optical propagation than fluorene. Moreover, the two polymorphs CPs **5a** and **5b** show very similar α_{dB} values, 0.867 and 0.875 dB mm^{-1}, respectively. This indicates that the OL is much more significantly influenced by variation in the chemical composition and connectivity rather than by changes in the molecular arrangement within the crystal lattice. Finally, a comparison of the α_{dB} values for the isostructural **L2**-based CPs **5a** and **6** reveals that the OL is halved on passing from the former to the latter, which exhibited the best optical propagation performance among the tested CPs. Worthy of note, the CPs featuring ethoxy-substituted moieties (e.g., **4** and **6**) exhibit better optical

https://doi.org/10.1021/jacsau.4c00978
JACS Au XXXX, XXX, XXX−XXX

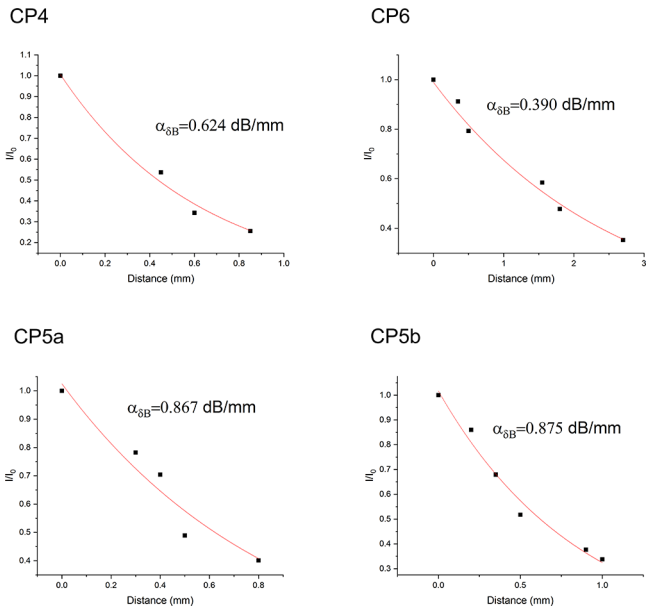

Figure 7. Optical waveguiding properties of CPs **4**, **5a**, **5b**, and **6**.

performance as compared to CPs **5a** and **5b**, which feature methoxy groups.

It is worth underlining that the estimated values of α_{dB} are among the smallest ever reported for CPs-based optical waveguides,[13,18] being even smaller than those determined for the majority of organic-based waveguides.[14] These results indicate that CPs **4**, **5a**, **5b**, and **6** exhibit a high degree of crystallinity, smooth surfaces, defect-free packing, and good light propagation performance. The α_{dB} values previously determined for Cu-based CPs ranged between 80 and 411 dB mm^{-},[1] with values depending on the mechanical stress applied to the crystals.[13]

A better performance was observed in the case of an Eu-based CP,[18] which exhibited an α_{dB} value of 8.94 dB mm^{-1}. This value is still one order of magnitude higher than that observed in the systems reported in the present study.

CONCLUSIONS

In order to investigate the influence of the structural features on their relative performance as active optical waveguides, a series of luminescent coordination polymers (CPs) based on closed-shell cadmium(II) ions were prepared by reacting **L1** and **L2** toward complexes **1** and **2** to form CPs **3**−**6**. The obtained CPs present analogous chemical connectivity around the Cd^{II} ion, exhibiting similar bond lengths, angles, and similar self-assembled sinusoidal zigzag chains with almost identical Cd···Cd distances. Three out of the five reported CPs were found to be isostructural, specifically **4**, **5a**, and **6**, and an interesting case of polymorphism was observed for CPs **5a** and **5b**. These similarities account for the excellent structural adaptability of fluorescent spacers **L1** and **L2**, confirming their potential as building blocks for the predictable assembly of fluorescent polymeric networks with controlled and tunable architectures.

The absorption and emission properties of **L1**, **L2**, and the resulting CPs were subjected to a comprehensive experimental and theoretical investigation. This revealed that the excitations contributing to the vertical transitions responsible for the broad, intense visible absorption in the Cd^{II}-based CPs are ligand-centered and involve the same frontier orbital responsible for the visible absorption of free ligands **L1** and **L2**. This provides an explanation for the analogous experimental optical behavior observed in the ligands and CPs, as well as the blue shift that occurs on passing from the free ligands to the corresponding CPs.

Focusing the attention on the PL properties of the three isostructural CPs (**4**, **5a** and **6**), their potential as optical waveguides was tested, with a particular emphasis on Optical Loss (OL). The measured α_{dB} values were found to be among the smallest ever reported for CPs-based and organic-based crystal waveguides. The differences in the measured values allowed us to make a few observations within the class of Cd^{II}−CPs: (i) CPs with the fluorenone moiety (**5** and **6**) are better at promoting light propagation than those with the fluorene moiety (CP **4**); (ii) The two polymorphs CPs **5a** and **5b** show similar α_{dB} values, indicating that in these systems, chemical connectivity plays a more a significant role in determining photoluminescence properties than molecular arrangements in the crystal packing. This is supported by the fact that CPs **5a** and **6** outperform CP **4**, with CP **6** demonstrating the best performance among the studied CPs, with α_{dB} = 0.390 dB mm^{-1}.

Further studies are currently underway in our laboratory, with the objective of preparing analogous supramolecular systems and evaluating their performance as optical waveguides.

METHODS

Materials

Chemicals, reagents, and solvents were purchased and used as received without any further purification unless otherwise stated. Diethylamine was distilled with $LiAlH_4$ and degassed before use. Toluene was distilled over Na and stored on molecular sieves. Melting point measurements were made in capillaries using a FALC melting point apparatus mod. C. (up to 300 °C). Elemental analyses were performed with an EA1108 CHNS-O Fisons instrument. NMR measurements were carried out at 25 °C in DMSO-d_6 using either a Bruker Avance 300 or an Avance III 400 or an Avance III HD 600 Hz spectrometer. Chemical shifts are reported in ppm (δ) and were calibrated to the solvent residue. Coupling constants J are given in Hertz (Hz). *In situ* micro-Raman scattering measurements were carried out in back scattering geometry with the 1064 nm line of a Nd:YAG laser. Measurements were performed in air at room temperature with a compact spectrometer B and WTEK (Newark-USA) i-Raman Ex integrated system with a spectral resolution of 8 cm^{-1}. For each experimental setup, all the spectra were collected with an acquisition time of about 30 s and power excitation between 20 and 40 mW concentrated in a spot of 0.3 mm^2 on the surface through a Raman Video Microsampling System (Nikon Eclipse for high-resolution and BAC151B in the other case) equipped with a 20× Olympus objective to select the area on the samples.

Absorption and Emission Spectroscopies

UV−visible measurements in solution were recorded in the range 190−1100 nm using quartz cuvettes with a path length of 1 cm by means of an Agilent Cary 5000 UV−vis−NIR dual-beam spectrophotometer. Diffuse reflectance measurements were carried out using either an Agilent Cary 5000 UV−vis−NIR dual-beam spectrophotometer equipped with a diffuse reflectance accessory or a Jasco V-750 spectrophotometer.

The solid-state absorption spectra have been obtained from the diffuse reflectance measurements applying the well-know Kubelka−Munk formula:

https://doi.org/10.1021/jacsau.4c00978
JACS Au XXXX, XXX, XXX−XXX

$$F(R_\infty) = \frac{K}{S} = \frac{(1 - R_\infty)^2}{2R_\infty}$$

$$R_\infty = \frac{R_{sample}}{R_{St}}$$

where R_{Sample} and R_{St} are the diffuse reflectance of the sample and the standard sample ($BaSO_4$ in the present case), respectively. K and S are the Kubelka–Munk absorption and scattering functions, respectively.

Photoluminescence emission spectra in solution and in the solid-state were collected with either a Varian Cary Eclipse spectrofluorometer or a PerkinElmer LS55 fluorescence spectrometer. Three-dimensional fluorescence mapping of samples was performed using a Jasco FP-8050 spectrofluorometer equipped with a 450 W xenon lamp as the excitation source. The maps were collected in the excitation range of 240–500 nm and an emission range of 350–800 nm with a 5 nm spectral bandwidth for excitation and emission. The optical waveguiding experiments were performed using a 450 nm diode as the excitation source. The PL intensities were recorded at the terminal point of each sample (I_{fin}) and normalized for the intensity registered at the entrance point (I_{ent}). The collected data can be represented by the exponential law:

$$I_{fin} = I_{ent} e^{-\alpha_{dB} D}$$

where D is the distance between the illuminated point and the collected point (that is the length of each sample) and α_{dB} is the loss coefficient. The absorption loss equation is derived from the Beer–Lambert law, where α_{dB} (in dB/mm) is related to the absorption coefficient as

$$\alpha_{dB} = 10\mathrm{Log}_{10}e(\alpha) = 4.34\alpha$$

For time-resolved photoluminescence (TR-PL), the measurements were performed by exciting the samples with 200 fs long pulses delivered by an optical parametric amplifier (Light Conversion TOPAS-C) pumped by a regenerative Ti:Sapphire amplifier (Coherent Libra-HE, Coherent Inc., Santa Clara, CA, USA). The repetition frequency was 1 kHz, and the PL signal was recovered by a streak camera (Hamamatsu C10910, Hamamatsu Photonics, Hamamatsu City, Shizuoka Pref., Japan) equipped with a grating spectrometer (Princeton Instruments Acton SpectraPro SP-2300, Teledyne Princeton Instruments, Trenton, NJ, USA).

X-ray Diffraction

Single-crystal X-ray diffraction data of **L1** were collected at 100 K on a Rigaku 007HF diffractometer equipped with Varimax confocal mirrors and an AFC11 goniometer and HyPix 6000 detector and data for **2**, collected at 120 K, on a Bruker-Nonius FR591, equipped with a κ-goniostat and Bruker-Nonius 95 mm CCD camera. SC-XRD data of CPs **3** and **4** were collected at 100 K on a Rigaku FRE+ diffractometer equipped with HF Varimax confocal mirrors, an AFC12 goniometer, and HG Saturn 724+ detector. X-ray structural determination of CPs **5a**, **5b** and **6** were carried out at 298 K and data collected on a Bruker D8 Venture diffractometer equipped with a PHOTON II detector. The structures were solved with the ShelXT[49] solution program using dual methods, and the models were refined with ShelXL 2018/3[50] using full-matrix least-squares minimization on F^2. Olex2 1.5[51] was used as the graphical interface. All hydrogen atoms were added in calculated positions and refined in riding positions relative to those of the parent atom. X-ray powder diffraction patterns were collected at room temperature using a Bruker D8 Advance diffractometer employing a Cu $K\alpha$ (λ = 1.54060 Å) radiation and the tube voltage and current set to 40 kV and 40 mA, respectively. The diffractometer was equipped with a Lynxeye XE-T detector operating in high-resolution 1D continuous mode. Hand-grinded samples were loaded on a zero-background Si specimen holder and analyzed using coupled $\theta/2\theta$ scans in the angular range of 5–50° (2θ) and a step size of 0.02°.

Theoretical Calculations

Theoretical calculations were carried out on fluorene, fluorenone, **L1**, **L2**, and the complex models **7** and **8** at the density functional theory (DFT) level by using the Gaussian 16 commercial suite of computational software.[52] Based on a previous investigation on related compounds,[20] the parameter-free PBE0 functional[43] was used for all calculations. The results obtained with the 6–311+G Pople basis sets[45,46] and Weigend Def2-SVP BSs[44] were compared. For all of the compounds, tight SCF convergence criteria and fine numerical integration grids were used. Optimized geometries were verified by harmonic frequency calculations, including the determination of thermochemistry parameters and calculation of FT-Raman frequencies. A complete natural population analysis (NPA) and the calculation of Wiberg bond indexes[48] were carried out with the natural bond orbital (NBO)[53] partitioning scheme to investigate the charge distributions.[54] Absorption and emission energies were calculated as described previously,[41] with the approximation of considering $ZPE^{GS} \approx ZPE^{ES} \ll E_{fluo}$. The vertical excitation energies used to interpret UV–vis absorption spectra (E_{abs}) were calculated by using the TD-DFT procedure on the ground state (GS) optimized geometries. The emission from the excited to the ground state, reflected in fluorescent emission (E_{fluo}), were computed analogously by adopting the optimized excited-state (ES) structure. By adopting the previously mentioned approximation, the adiabatic excitation energies (E_{adia}) and the corresponding excitation wavelengths (λ_{adia}) were calculated as the difference between the ground and excited state energies obtained in their corresponding optimized geometries. For all molecules, the first singlet excited state was considered in the emission processes. The bulk solvent effects were implicitly taken into account by means of nonequilibrium Polarizable Continuum Model in its Integral Equation Formalism (IEF-PCM), describing the cavity of the complexes within the self-consistent reaction field (SCRF) through a set of overlapping spheres. UV–vis spectra (Figure S14 for **L2**) were simulated as the convolution of Gaussian-shaped curves, centered at the TD-DFT-calculated absorption energy with a fixed halfbandwidth (width of the band at half height) of 25 nm and a height proportional to the calculated oscillator strength.[55] GaussView 6.0.16[56] was used to analyze Kohn–Sham (KS) molecular orbital (MO) compositions and energies. Chemissian 4.54[57] was used to evaluate the atomic orbital contributions to KS-MOs and to analyze the contribution of one-electron excitations to molecular transitions. All calculations were carried out using a CINECA Galileo100 supercomputer.

Syntheses

L2 and complex **1** were synthesized as previously described.[29,58,59]

Synthesis of 2,7-Bis(pyridin-3-ylethynyl)-9H-fluorene (L1). 3-ethynylpyridine (517 mg; 5.01 mmol), 2,7-dibromofluorene (806 mg; 2.49 mmol), copper iodide (24 mg; 0.13 mmol), and $Pd(PPh_3)_2Cl_2$ (90 mg; 0.13 mmol) were placed in a 50 mL three-necked round-bottom flask that was evacuated and refilled three times with dry nitrogen. Dry toluene (20 mL) and freshly distilled and degassed diethylamine (10 mL) were added via canula and the mixture was heated to reflux and kept under a nitrogen atmosphere for 48 h. After the mixture cooled to room temperature, the precipitate was filtered off and the solution treated with saturated NH_4Cl solution (50 mL) and extracted with ethyl acetate (3 × 25 mL). The organic phase was dried over $MgSO_4$, filtered, and concentrated. The two isolated solids were combined and purified by silica gel column chromatography using a gradient of CH_2Cl_2/EtOAc as eluent (light-yellow solid; 344 mg; 9.34×10^{-4} mol; yield 37%) Mp = 107 °C. TOF MS ES(+): $[M + H]^+$ $C_{27}H_{17}N_2^+$ (m/z): calcd 369.1362; found 369.1402; $[M+CH_3CN+H]^+$ $C_{29}H_{20}N_3^+$calcd 410.1652; found 410.1656 m/z. Elemental analysis calcd (%) for $C_{27}H_{16}N_2$: C 88.02, H 4.38, N 7.60. Found: C 87.79, H 4.12, N 7.31. Raman (2500–500 cm^{-1}): 541w, 605w, 755m, 816w, 1036m, 1099s, 1179m, 1195m, 1229m, 1273m, 1328s, 1414w, 1477w, 1581ms, 1607vs, 2208s cm^{-1}. ^1H NMR (400 MHz, DMSO-d_6) δ 8.79 (m, 2H, Py), 8.60 (dd, J = 4.9, 1.6 Hz, 2H, Py), 8.05 (d, J = 7.8 Hz, 2H, fluorene), 8.01 (dt, J = 8.0, 1.6 Hz, 2H, Py), 7.85 (m, 2H, fluorene),

https://doi.org/10.1021/jacsau.4c00978
JACS Au XXXX, XXX, XXX–XXX

7.66 (dd, J = 7.8, 1.4 Hz, 2H, fluorene), 7.49 (dd, J = 8.0, 4.9 Hz, 2H, Py), 4.03 (s, 2H, CH2) ppm. $^{13}C\{^1H\}$-NMR (101 MHz, DMSO-d6) δ: 151.59, 148.96, 143.96, 141.15, 138.48, 130.58, 128.29, 123.66, 120.98, 120.35, 119.50, 93.01, 86.56, 36.21 ppm.

Synthesis of Complex *1*. Lawesson's reagent (404 mg; 1.0 mmol) and $Cd(NO_3)_2{\cdot}4H_2O$ (308 mg; 1.0 mmol) were dissolved in methanol (20 mL) and the reaction mixture was heated to reflux for 2 h. The precipitate was filtered and purified by recrystallization from a 4:1 dichloromethane/methanol mixture to give the pure product as colorless crystals (439 mg; 0.38 mmol, yield 85% based on $C_{32}H_{40}Cd_2O_8P_4S_8$). Mp = 151 °C. Elemental analysis calcd (%) for $C_{32}H_{40}Cd_2O_8P_4S_8$: C = 33.19, H = 3.48, S = 22.15. Found: C = 33.18, H = 3.57, S = 22.06. Raman (2500−500 cm^{-1}): 547s, 630m, 661mw, 773m, 804ms, 1012w, 1116s, 1184w, 1257w, 1301w, 1456w, 1592s cm^{-1}. ^1H NMR (600 MHz, DMSO-d_6) δ 7.94−7.82 (m, 8H), 7.01 (dd, $^4J_{P\text{-}H}$ = 2.8 Hz, $^3J_{H\text{-}H}$ = 8.8 Hz, 8H) 3.80 (s, 12H, Ar-OMe), 3.69 (d, $^2J_{P\text{-}H}$ = 15.2 Hz, 12H, P-OMe) ppm. $^{13}C\{^1H\}$-NMR (151 MHz, DMSO-d_6) δ: 161.18, 161.16, 131.63, 131.54, 113.28, 113.18, 55.34, 51.04, 51.00 ppm.

Synthesis of Complex 2. Lawesson's Reagent (404 mg; 1.0 mmol) and $Cd(NO_3)_2{\cdot}4H_2O$ (308 mg; 1.0 mmol) were placed in a 50 mL round-bottom flask, and ethanol (20 mL) was added in one portion. The mixture was heated to reflux for 2 h, and the progressive precipitation of a white solid was observed. The mixture was cooled to room temperature and the precipitate was filtered on a Gooch funnel. The white powder was then washed with hot ethanol and dried under vacuum. Colorless crystals suitable for X-ray diffraction analysis were grown by slow evaporation from a chloroform solution of the product (272 mg; 0.22 mmol; yield 45%) Mp = 150 °C. Elemental analysis calcd (%) for $C_{36}H_{48}Cd_2O_8P_4S_8$: C 35.62, H 3.98, S 21.13. Found: C 35.21, H 3.54, S 20.97. Raman (2500−500 cm^{-1}): 541s, 630w, 661w, 804s, 1012w, 1116s, 1184w, 1268w, 1311w, 1456w, 1597s cm^{-1}. ^1H-NMR (600 MHz, DMSO-d_6) δ 7.88 (dd, $^3J_{P\text{-}H}$ = 13.8 Hz, $^3J_{H\text{-}H}$ = 8.8 Hz, 8H), 7.00 ($^3J_{H\text{-}H}$ = 8.8 Hz, $^4J_{P\text{-}H}$ = 2.6 Hz, 8H), 4.13 (dq, $^3J_{P\text{-}H}$ = 9.6 Hz, $^3J_{H\text{-}H}$ = 7.1 Hz, 8H), 3.80 (s, 12H, Ar-OMe), 1.24 (t, $^3J_{H\text{-}H}$ = 7.1 Hz, 12H) ppm. $^{13}C\{^1H\}$-NMR (151 MHz, DMSO-d_6) δ: 161.12, 131.57, 131.48, 113.25, 113.15, 60.33, 55.33, 16.11, 16.05 ppm.

General Method Followed for the Preparation of CPs 3−6. The syntheses of the CPs presented in this study were performed in triplicate in 8 mL glass vials with screwcaps as follows: a solution of ligand (**L1** or **L2**) in chloroform (5 mM; 2 mL) was added to an alcoholic solution (MeOH or EtOH) of complex **1** or **2** (5 mM; 2 or 2.5 mM; 4 mL). The resulting solution was placed in an ultrasonic bath (120 W) for 10 min, filtered through a 0.45 μm PTFE filter, and allowed to evaporate slowly at room temperature. The crystalline products formed within 24−48 h were isolated from the solution, gently washed with the corresponding alcohol (MeOH for CPs **3** and **4**, EtOH for CPs **5** and **6**), and air-dried.

Synthesis of CP 3. Colorless plate-shaped crystals. Mp = 156 °C. Elemental analysis calcd (%) for $C_{43}H_{36}CdN_2O_4P_2S_4{\cdot}CHCl_3$: C = 49.54, H = 3.41, N = 2.63, S = 12.02. Found: C = 49.21, H = 3.37, N = 2.48, S = 11.83. Raman (2500−500 cm^{-1}): 547w, 611w, 668w, 755w, 822w, 1030m, 1099ms, 1184ms, 1229m, 1419w, 1488w, 1592s, 1607vs, 2213s cm^{-1}.

Synthesis of CP 4. Light-yellow rod-shaped crystals Mp = 161 °C. Elemental analysis calcd (%) for $C_{45}H_{40}CdN_2O_4P_2S_4$: C = 55.41, H = 4.13, N = 2.87, S = 13.15. Found: C = 55.24, H = 3.98, N = 2.66, S = 13.01. Raman (2500−500 cm^{-1}): 547w, 611w, 755w, 822w, 1030m, 1099 ms, 1184ms, 1229m, 1419w, 1488w, 1592s, 1607vs, 2213s cm^{-1}.

Synthesis of CP 5: 5a/5b. Following the generic protocol stated above, the simultaneous formation of CP **5a** (yellow lath-shaped crystals) and CP **5b** (yellow tablet-shaped crystals) was observed. CP **5a**: Mp = 173 °C. Elemental analysis calcd (%) for $C_{43}H_{34}CdN_2O_5P_2S_4$: C = 53.72, H = 3.56, N = 2.91, S = 13.34. Found: C = 53.68, H = 3.44, N = 2.82, S = 13.27. Raman (2500−500 cm^{-1}): 541w, 586w, 798w, 1030m, 1070mw, 1076m, 1116m, 1173s, 1184m, 1286w, 1333m, 1425m, 1602vs, 1727w, 2213 ms ($\nu C{\equiv}C$) cm^{-1}. CP **5b**: Mp = 154 °C. Elemental analysis calcd (%) for $C_{43}H_{34}CdN_2O_5P_2S_4$: C = 53.72, H = 3.56, N = 2.91, S = 13.34. Found: C = 53.75, H = 3.52, N = 2.87, S = 13.38. Raman (2500−500 cm^{-1}): 541w, 586w, 798w, 1030m, 1047w, 1076m, 1122w, 1173s, 1207m, 1268w, 1333m, 1425m, 1602vs, 1723w, 2217 ms cm^{-1}.

Synthesis of CP 6. Yellow lath-shaped crystals. Mp = 186 °C. Elemental analysis calcd (%) for $C_{45}H_{38}CdN_2O_5P_2S_4$: C = 54.63, H = 3.87, N = 2.83, S = 12.96. Found: C = 54.55, H = 3.83, N = 2.76, S = 13.01. Raman (2500−500 cm^{-1}): 547w, 586w, 1030m, 1076m, 1116w, 1173s, 1268w, 1333m, 1425m, 1602s, 1727w, 2213ms cm^{-1}.

■ ASSOCIATED CONTENT

Supporting Information

The Supporting Information is available free of charge at https://pubs.acs.org/doi/10.1021/jacsau.4c00978.

SCXRD and PXRD analysis, absorption and emission spectroscopies, TD-DFT calculations, NMR, MS, Raman. Crystallographic data have been deposited at the Cambridge Crystallographic Data Centre (CCDC) under deposition numbers: 2388747−2388753 (PDF)

■ AUTHOR INFORMATION

Corresponding Authors

Enrico Podda − *Dipartimento di Scienze Chimiche e Geologiche, Università degli Studi di Cagliari, Cittadella Universitaria, Monserrato − Cagliari 09042, Italy; Centro Servizi di Ateneo per la Ricerca − CeSAR, Università degli Studi di Cagliari, Cittadella Universitaria, Monserrato − Cagliari 09042, Italy*; Email: enrico.podda@unica.it

M. Carla Aragoni − *Dipartimento di Scienze Chimiche e Geologiche, Università degli Studi di Cagliari, Cittadella Universitaria, Monserrato − Cagliari 09042, Italy;* orcid.org/0000-0002-5010-7370; Email: aragoni@unica.it

Authors

Massimiliano Arca − *Dipartimento di Scienze Chimiche e Geologiche, Università degli Studi di Cagliari, Cittadella Universitaria, Monserrato − Cagliari 09042, Italy;* orcid.org/0000-0002-0058-6406

Anna Pintus − *Dipartimento di Scienze Chimiche e Geologiche, Università degli Studi di Cagliari, Cittadella Universitaria, Monserrato − Cagliari 09042, Italy;* orcid.org/0000-0001-6069-9771

Vito Lippolis − *Dipartimento di Scienze Chimiche e Geologiche, Università degli Studi di Cagliari, Cittadella Universitaria, Monserrato − Cagliari 09042, Italy;* orcid.org/0000-0001-8093-576X

Simon J. Coles − *UK National Crystallography Service, School of Chemistry, Faculty of Engineering and Physical Sciences, University of Southampton, University of Southampton SO17 1BJ, United Kingdom;* orcid.org/0000-0001-8414-9272

James B. Orton − *UK National Crystallography Service, School of Chemistry, Faculty of Engineering and Physical Sciences, University of Southampton, University of Southampton SO17 1BJ, United Kingdom*

Stefania Porcu − *Dipartimento di Fisica, Università degli Studi di Cagliari, Cittadella Universitaria, Monserrato − Cagliari 09042, Italy*

Pier Carlo Ricci − *Dipartimento di Fisica, Università degli Studi di Cagliari, Cittadella Universitaria, Monserrato − Cagliari 09042, Italy;* orcid.org/0000-0001-6191-4613

Complete contact information is available at: https://pubs.acs.org/10.1021/jacsau.4c00978

https://doi.org/10.1021/jacsau.4c00978
JACS Au XXXX, XXX, XXX−XXX

Author Contributions

E.P. and M.C.A. designed, supervised the whole research and wrote the original version of the manuscript. M.A. carried out the theoretical investigation. S.J.C.,J.B.O. and E.P. collected, processed and analyzed structural data. A.P. and V.L. contributed to data curation, writing and editing. S.P. and P.C.R. performed the absorption and emission spectroscopic studies. All authors have given approval to the final version of the manuscript. CRediT: **Enrico Podda** conceptualization, data curation, formal analysis, investigation, methodology, validation, writing - original draft, writing - review & editing; **Massimiliano Arca** conceptualization, data curation, formal analysis, writing - review & editing; **Anna Pintus** data curation, writing - review & editing; **Vito Lippolis** data curation, writing - review & editing; **Simon J. Coles** data curation, investigation; **James B. Orton** data curation, investigation; **Stefania Porcu** data curation, investigation, methodology; **Pier Carlo Ricci** data curation, investigation, methodology, writing - original draft; **Maria Carla Aragoni** conceptualization, data curation, formal analysis, investigation, methodology, supervision, validation, visualization, writing - original draft, writing - review & editing.

Notes

The authors declare no competing financial interest.

■ ACKNOWLEDGMENTS

The authors kindly acknowledge CINECA for the computational resources on the Galileo100 supercomputer accessed within the ISCRA project BIFluoex, the, and CeSAR − University of Cagliari (Italy) for giving access to XRD and ultrafast optical spectroscopy facilities. The authors acknowledge the Ministero per l'Ambiente e la Sicurezza Energetica (MASE; formerly Ministero della Transizione Ecologica, MITE) − Direzione generale Economia Circolare for funding (Progetti di ricerca finalizzati allo sviluppo di nuove tecnologie per il recupero, il riciclaggio, il trattamento di rifiuti di apparecchiature elettriche ed elettroniche RAEE − Edizione 2021). Fondazione di Sardegna (FdS Progetti Biennali di Ateneo, annualità 2022) is kindly acknowledged for financial support. The authors kindly acknowledge Daniele Mele (https://danielemele.my.canva.site/hello) for the realization of the cover artwork related to this work.

■ REFERENCES

(1) Liu, J.-M. Optical Waveguides. In *Photonic Devices*; Cambridge University Press, 2005, pp. 73−118. .

(2) Tian, D.; Chen, Y. Optical Waveguides in Organic Crystals of Polycyclic Arenes. *Adv. Opt. Mater.* **2021**, *9* (23), 2002264.

(3) Annadhasan, M.; Karothu, D. P.; Chinnasamy, R.; Catalano, L.; Ahmed, E.; Ghosh, S.; Naumov, P.; Chandrasekar, R. Micromanipulation of Mechanically Compliant Organic Single-Crystal Optical Microwaveguides. *Angew. Chem. Int. Ed.* **2020**, *59* (33), 13821−13830.

(4) Law, M.; Sirbuly, D. J.; Johnson, J. C.; Goldberger, J.; Saykally, R. J.; Yang, P. Nanoribbon Waveguides for Subwavelength Photonics Integration. *Science* **2004**, *305* (5688), 1269−1273.

(5) Pan, A.; Liu, D.; Liu, R.; Wang, F.; Zhu, X.; Zou, B. Optical Waveguide through CdS Nanoribbons. *Small* **2005**, *1* (10), 980−983.

(6) Wang, Z.; Liu, J.; Xu, Z. Q.; Xue, Y.; Jiang, L.; Song, J.; Huang, F.; Wang, Y.; Zhong, Y. L.; Zhang, Y.; Cheng, Y. B.; Bao, Q. Wavelength-Tunable Waveguides Based on Polycrystalline Organic−Inorganic Perovskite Microwires. *Nanoscale* **2016**, *8* (12), 6258−6264.

(7) Wang, Z.; Han, W.; Shi, R.; Han, X.; Zheng, Y.; Xu, J.; Bu, X. H. Mechanoresponsive Flexible Crystals. *JACS Au* **2024**, *4* (2), 279−300.

(8) Chandrasekar, R. Mechanophotonics − a Guide to Integrating Microcrystals toward Monolithic and Hybrid All-Organic Photonic Circuits. *Chem. Commun.* **2022**, *58* (21), 3415−3428.

(9) Bhattacharya, B.; Michalchuk, A. A. L.; Silbernagl, D.; Rautenberg, M.; Schmid, T.; Feiler, T.; Reimann, K.; Ghalgaoui, A.; Sturm, H.; Paulus, B.; Emmerling, F. A Mechanistic Perspective on Plastically Flexible Coordination Polymers. *Angew. Chem., Int. Ed.* **2020**, *59* (14), 5557−5561.

(10) An, L. C.; Li, X.; Li, Z. G.; Li, Q.; Beldon, P. J.; Gao, F. F.; Li, Z. Y.; Zhu, S.; Di, L.; Zhao, S.; Zhu, J.; Comboni, D.; Kupenko, I.; Li, W.; Ramamurty, U.; Bu, X. H. Plastic Bending in a Semiconducting Coordination Polymer Crystal Enabled by Delamination. *Nat. Commun.* **2022**, *13* (1), 1−9.

(11) Panda, M. K.; Ghosh, S.; Yasuda, N.; Moriwaki, T.; Mukherjee, G. D.; Reddy, C. M.; Naumov, P. Spatially Resolved Analysis of Short-Range Structure Perturbations in a Plastically Bent Molecular Crystal. *Nat. Chem.* **2015**, *7* (1), 65−72.

(12) Barman, D.; Annadhasan, M.; Bidkar, A. P.; Rajamalli, P.; Barman, D.; Ghosh, S. S.; Chandrasekar, R.; Iyer, P. K. Highly Efficient Color-Tunable Organic Co-Crystals Unveiling Polymorphism, Isomerism, Delayed Fluorescence for Optical Waveguides and Cell-Imaging. *Nat. Commun.* **2023**, *14* (1), 1−17.

(13) Panbarasu, S.; Khapre, A.; Chosenyah, M.; Kumar, A. V.; Chandrasekar, R. Highly Strained Pseudoplastic, Cu-Pyridyl Coordination Polymer Crystal-Based Optical Waveguide Cavity. *Chem. Mater.* **2023**, *35* (23), 10169−10177.

(14) Liu, H.; Lu, Z.; Zhang, Z.; Wang, Y.; Zhang, H. Highly Elastic Organic Crystals for Flexible Optical Waveguides. *Angew. Chem., Int. Ed.* **2018**, *57* (28), 8448−8452.

(15) Cao, X.; Peng, J.; Wang, W.; Xu, W.; Xu, S. An Elastic Luminescent Organic Single Crystal with Linear and Nonlinear Optical Waveguide Properties. *Dyes Pigm.* **2023**, *219*, 111531.

(16) Sun, C. L.; Gao, Z.; Teng, K. X.; Niu, L. Y.; Chen, Y. Z.; Zhao, Y. S.; Yang, Q. Z. Supramolecular Polymer-Based Fluorescent Microfibers for Switchable Optical Waveguides. *ACS Appl. Mater. Interfaces* **2018**, *10* (31), 26526−26532.

(17) Pisačić, M.; Kodrin, I.; Trninić, A.; Da-Ković, M. Two-Dimensional Anisotropic Flexibility of Mechanically Responsive Crystalline Cadmium(II) Coordination Polymers. *Chem. Mater.* **2022**, *34* (5), 2439−2448.

(18) Song, M.; Dang, Y.; Dong, J.; Zhang, X.; Lei, S.; Hu, W. Eu-Based Coordination Polymer Microrods for Low-Loss Optical Waveguiding Application. *Nanoscale* **2019**, *11* (44), 21061−21067.

(19) Su, S.; Qin, C.; Guo, Z.; Guo, H.; Song, S.; Deng, R.; Cao, F.; Wang, S.; Li, G.; Zhang, H. Five Three/Two-Fold Interpenetrating Architectures from Self-Assembly of Fluorene-2,7-Dicarboxylic Acid Derivatives and d^{10} Metals. *CrystEngComm* **2011**, *13* (8), 2935−2941.

(20) Podda, E.; Arca, M.; Pintus, A.; Lippolis, V.; Caltagirone, C.; Coles, S.; Orton, J. B.; Ennas, G.; Picci, G.; Davies, R.; Aragoni, M. C. On the Role of Torsional Dynamics in the Solid-State Fluorescent Properties of a New Bifluorene-Tetracarboxylic Acid and Its Supramolecular Assemblies: A Structural and TD-DFT Investigation. *CrystEngComm* **2023**, *25*, 1058−1066.

(21) Pschirer, N. G.; Ciurtin, D. M.; Smith, M. D.; Bunz, U. H. F.; Loye, H.-C. Z. Noninterpenetrating Square-Grid Coordination Polymers With Dimensions of 25 × 25 $Å^2$ Prepared by Using N,N′-Type Ligands: The First Chiral Square-Grid Coordination Polymer. *Angew. Chem., Int. Ed.* **2002**, *41* (4), 583−585.

(22) Ciurtin, D. M.; Pschirer, N. G.; Smith, M. D.; Bunz, U. H. F.; Zur Loye, H. C. Two Luminescent Coordination Polymers with a Triple-Helix Structure: $HgX_2(C_{31}H_{24}N_2)\cdot CH_2Cl_2$ (X = Cl and Br). *Chem. Mater.* **2001**, *13* (9), 2743−2745.

(23) Li, D. Y.; Xie, H.; Yao, X. Q.; Ma, H. C.; Lei, Z. Q.; Liu, J. C. A Luminescent Coordination Polymer Based on a π-Conjugated Ligand: Syntheses, Structure and Luminescent Property. *J. Mol. Struct.* **2017**, *1134*, 171−173.

https://doi.org/10.1021/jacsau.4c00978
JACS Au XXXX, XXX, XXX−XXX

(24) Chen, Z.; Sun, Y.; Liu, Z. A.; Wang, N.; Yang, X.; You, X.; Wang, X. A Three-Dimensional Zn^{II} Coordination Network Based on 5,5′-Methylenebis(2,4,6-Trimethylisophthalic Acid) and 2,7-Bis(1H-Imidazol-1-Yl)Fluorene: Synthesis, Structure and Luminescence Properties. *Acta Crystallogr.* **2019**, *75* (1), 8−14.
(25) Sun, S.; Sun, Y.; Guo, H.; Fu, X.; Guo, M.; Liu, S.; Guo, X.; Zhang, L.; Alexandrov, E. V. Construction of Cd(II) Coordination Polymers from a Fluorene-Based Bisimidazole Ligand and Polycarboxylic Acids: Syntheses, Structures and Properties. *Inorg. Chim. Acta.* **2018**, *483*, 165−172.
(26) Zhao, L.; XinLiu; Zhao, C.; Meng, L. Synthesis and Properties of Interspersed Structure Complexes Prepared from 4,4′-(Phenylazanediyl)-Dibenzoic Acid with Rigid and Semi-Rigid Nitrogen-Containing Ligands. *J. Mol. Struct.* **2019**, *1180*, 547−555.
(27) Liu, Y.-F.; Zhao, C.-W.; Ma, J.-P.; Liu, Q.-K.; Dong, Y.-B. The Coordination Chemistry of Two Symmetric Fluorene-Based Organic Ligands with Cuprous Chloride. *Acta Crystallogr.* **2013**, *69* (12), 1488−1493.
(28) Podda, E.; Arca, M.; Pintus, A.; Meloni, F.; Lippolis, V.; Ferino, G.; Orton, J. B.; Coles, S. J.; Aragoni, M. C. 2-(2,7-Bis(Pyridin-3-Ylethynyl)Fluoren-9-Ylidene)Malononitrile. *Molbank* **2023**, *2023* (2), M1619.
(29) Podda, E.; Arca, M.; Pintus, A.; Demontis, V.; Lippolis, V.; Ferino, G.; Orton, J. B.; Coles, S. J.; Aragoni, M. C. 2,7-Bis(Pyridin-3-Ylethynyl)Fluoren-9-One. *Molbank* **2023**, *2023* (1), M1540.
(30) Aragoni, M. C.; Arca, M.; Cabras, V.; Coles, S. J.; Ennas, G.; Isaia, F.; Lai, R.; Lippolis, V.; Podda, E. Coordination Polymers Based on Dithiophosphato/Dithiophosphonato Nickel Complexes and Linear 1,4-Di(3-Pyridyl)Buta-1,3-Diyne Ligand. *Supramol. Chem.* **2017**, *29* (11), 853−864.
(31) Aragoni, M. C.; Arca, M.; Champness, N. R.; De Pasquale, M.; Devillanova, F. A.; Isaia, F.; Lippolis, V.; Oxtoby, N. S.; Wilson, C. Synthesis and Structural Characterisation of Coordination Polymers Designed Using Discrete Phosphonodithioato Ni^{II} Complexes and Dipyridyl Donor Ligands. *CrystEngComm* **2005**, *7*, 363−369.
(32) *See for Example CCDC Refcodes*; HAHDUQ, HAHFAY, SIXHUD, XALHUO, HAHDEA, MERXUD, QIDKOG.
(33) Aragoni, M. C.; Arca, M.; Crespo, M.; Devillanova, F. A.; Hursthouse, M. B.; Huth, S. L.; Isaia, F.; Lippolis, V.; Verani, G. Investigation on the Reactivity of Dithiophosphonato/Dithiophosphato Ni^{II} Complexes towards 2,4,6-Tris-2-Pyridyl-1,3,5-Triazine: Developments and New Perspectives. *Dalton Trans.* **2009**, *14*, 2510−2520.
(34) Aragoni, M. C.; Arca, M.; Demartin, F.; Devillanova, F. A.; Graiff, C.; Isaia, F.; Lippolis, V.; Tiripicchio, A.; Verani, G. Ring-Opening of Lawesson's Reagent: New Syntheses of Phosphono- and Ami-dophosphono-Dithioato Complexes − Structural and CP-MAS ^{31}P-NMR Characterization of $[p\text{-}CH_3OPh(X)PS_2]_2M$ (X = MeO, ^{i}PrNH; M = Ni^{II}, Pd^{II}, and Pt^{II}). *Eur. J. Inorg. Chem.* **2000**, *2000* (10), 2239−2244.
(35) van Zyl, W. E.; Woollins, J. D. The Coordination Chemistry of Dithiophosphonates: An Emerging and Versatile Ligand Class. *Coord. Chem. Rev.* **2013**, *257*, 718−731.
(36) Moula, G.; Bose, M.; Datta, H.; Sarkar, S. Photoluminescent Mo(IV) and W(IV) Bis-Dithiolene Complexes with Bidentate Phosphonodithioato Ligand Derived from Lawesson's Reagent. *Polyhedron* **2013**, *52*, 900−908.
(37) Semeniuc, R. F.; Reamer, T. J.; Blitz, J. P.; Wheeler, K. A.; Smith, M. D. Functionalized O-Alkyldithiocarbonates: A New Class of Ligands Designed for Luminescent Heterometallic Materials. *Inorg. Chem.* **2010**, *49* (6), 2624−2629.
(38) Tong, B.; Zhang, M.; Han, Z.; Mei, Q.; Zhang, Q. Novel Colorimetric Phosphorescent Chemodosimeter for Hg^{2+} Based Iridium(III) Complex with Phosphonodithioate Auxiliary Ligand. *J. Organomet. Chem.* **2013**, *724*, 180−185.
(39) van Zyl, W. E. Dithiophosphonates and Related P/S-Type Ligands of Group 11 Metals. *Comments Inorg. Chem.* **2010**, *31* (1−2), 13−45.
(40) Podda, E.; Arca, M.; Coles, S. J.; Crespo Alonso, M.; Isaia, F.; Pintus, A.; Lippolis, V.; Aragoni, M. C. Supramolecular Assemblies Tailored by Dipyridyl-1,2,4-Thiadiazoles: Influence of the Building Blocks in the Predictability of the Final Network. *Supramol. Chem.* **2020**, *32* (4), 267−275.
(41) Jacquemin, D.; Planchat, A.; Adamo, C.; Mennucci, B. TD-DFT Assessment of Functionals for Optical 0−0 Transitions in Solvated Dyes. *J. Chem. Theory Comput.* **2012**, *8* (7), 2359−2372.
(42) Ghosh, I.; Mukhopadhyay, A.; Koner, A. L.; Samanta, S.; Nau, W. M.; Moorthy, J. N. Excited-State Properties of Fluorenones: Influence of Substituents, Solvent and Macrocyclic Encapsulation. *Phys. Chem. Chem. Phys.* **2014**, *16* (31), 16436−16445.
(43) Adamo, C.; Barone, V. Toward Reliable Density Functional Methods without Adjustable Parameters: The PBE0Model. *J. Chem. Phys.* **1999**, *110* (13), 6158−6170.
(44) Weigend, F.; Ahlrichs, R. Balanced Basis Sets of Split Valence, Triple Zeta Valence and Quadruple Zeta Valence Quality for H to Rn: Design and Assessment of Accuracy. *Phys. Chem. Chem. Phys.* **2005**, *7* (18), 3297−3305.
(45) Krishnan, R.; Binkley, J. S.; Seeger, R.; Pople, J. A. Self-consistent Molecular Orbital Methods. XX. A Basis Set for Correlated Wave Functions. *J. Chem. Phys.* **1980**, *72* (1), 650−654.
(46) Clark, T.; Chandrasekhar, J.; Spitznagel, G. W.; Schleyer, P. V. R. Efficient Diffuse Function-Augmented Basis Sets for Anion Calculations. III. The 3-21+G Basis Set for First-Row Elements, Li−F. *J. Comput. Chem.* **1983**, *4* (3), 294−301.
(47) Tomasi, J.; Mennucci, B.; Cancès, E. The IEF Version of the PCM Solvation Method: An Overview of a New Method Addressed to Study Molecular Solutes at the QM Ab Initio Level. *J. Mol. Struct.:THEOCHEM* **1999**, *464* (1−3), 211−226.
(48) Wiberg, K. B. Application of the Pople-Santry-Segal CNDO Method to the Cyclopropylcarbinyl and Cyclobutyl Cation and to Bicyclobutane. *Tetrahedron* **1968**, *24* (3), 1083−1096.
(49) Sheldrick, G. M. SHELXT - Integrated Space-Group and Crystal-Structure Determination. *Acta Crystallogr.* **2015**, *A71* (1), 3−8.
(50) Sheldrick, G. M. Crystal Structure Refinement with SHELXL. *Acta Crystallogr.* **2015**, *C71* (1), 3−8.
(51) Dolomanov, O. V.; Bourhis, L. J.; Gildea, R. J.; Howard, J. A. K.; Puschmann, H. OLEX2: A Complete Structure Solution, Refinement and Analysis Program. *J. Appl. Crystallogr.* **2009**, *42* (2), 339−341.
(52) Frisch, M. J.; Trucks, G. W.; Schlegel, H. B.; Scuseria, G. E.; Robb, M. A.; Cheeseman, J. R.; Scalmani, G.; Barone, V.; Petersson, G. A.; Nakatsuji, H., et al. *2016*; *Gaussian 16, Rev. B.01*, Gaussian Inc.: Wallingford, CT, 2016.
(53) Reed, A. E.; Curtiss, L. A.; Weinhold, F. Intermolecular Interactions from a Natural Bond Orbital, Donor—Acceptor Viewpoint. *Chem. Rev.* **1988**, *88* (6), 899−926.
(54) Glendening, E. D.; Landis, C. R.; Weinhold, F. NBO 6.0: Natural bond orbital analysis program. *J. Computat. Chem.* **2013**, *34* (16), 1429−1437.
(55) Aragoni, M. C.; Area, M.; Crisponi, G.; Nurchi, V. M. Simultaneous Decomposition of Several Spectra into the Constituent Gaussian Peaks. *Anal. Chim. Acta.* **1995**, *316* (2), 195−204.
(56) Dennington, R. D.; Keith, T. A.; Millam, J. M. *GaussView 6.0. 16*; Semichem Inc.: Shawnee Mission KS, 2016.
(57) Skripnikov, L. V. *Chemissian Version 4.54*; Visualization Computer Program, 2017.
(58) Arca, M.; Cornia, A.; Devillanova, F. A.; Fabretti, A. C.; Isaia, F.; Lippolis, V.; Verani, G. New Perspectives in Phosphonodithioate Coordination Chemistry. Synthesis and X-Ray Crystal Structure of Trans-Bis-[O-Ethyl-(4-Methoxyphenyl)Phosphonodithioato] Nickel-(II). *Inorg. Chim. Acta.* **1997**, *262* (1), 81−84.
(59) Aragoni, M. C.; Arca, M.; Demartin, F.; Devillanova, F. A.; Grai, C.; Isaia, F.; Lippolis, V.; Tiripicchio, A.; Verani, G. Reactivity of Phosphonodithioato Ni^{II} Complexes: Solution Equilibria, Solid State Studies and Theoretical Calculations on the Adduct Formation with Some Pyridine Derivatives. *Dalton Trans.* **2001**, *18*, 2671−2677.

https://doi.org/10.1021/jacsau.4c00978
JACS Au XXXX, XXX, XXX−XXX